Boron carbide under torsional deformation: evidence of the formation of chain vacancies in the plastic regime

Amrita Chakraborti, Antoine Jay, Olivier Hardouin Duparc, Jelena Sjakste, Keevin Béneut, Nathalie Vast, Yann Le Godec

Journal Pre-proof

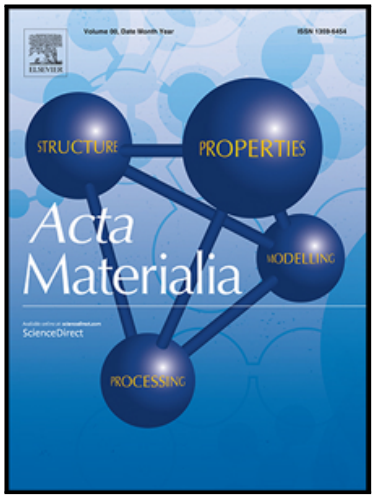

Boron carbide under torsional deformation: evidence of the formation of chain vacancies in the plastic regime

Amrita Chakraborti, Antoine Jay, Olivier Hardouin Duparc, Jelena Sjakste, Keevin Béneut, Nathalie Vast, Yann Le Godec

PII: S1359-6454(21)00931-9
DOI: https://doi.org/10.1016/j.actamat.2021.117553
Reference: AM 117553

To appear in: *Acta Materialia*

Received date: 10 August 2021
Revised date: 6 December 2021
Accepted date: 8 December 2021

Please cite this article as: Amrita Chakraborti, Antoine Jay, Olivier Hardouin Duparc, Jelena Sjakste, Keevin Béneut, Nathalie Vast, Yann Le Godec, Boron carbide under torsional deformation: evidence of the formation of chain vacancies in the plastic regime, *Acta Materialia* (2021), doi: https://doi.org/10.1016/j.actamat.2021.117553

Graphical Abstract

Boron carbide under torsional deformation: evidence of the formation of chain vacancies in the plastic regime

Amrita Chakraborti, Antoine Jay, Olivier Hardouin Duparc, Jelena Sjakste, Keevin Béneut, Nathalie Vast, Yann Le Godec

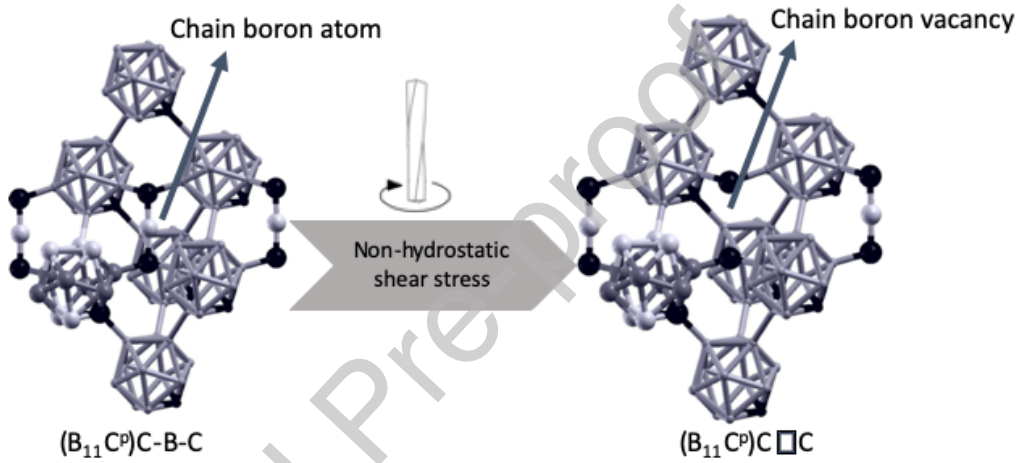

Highlights

Boron carbide under torsional deformation: evidence of the formation of chain vacancies in the plastic regime

Amrita Chakraborti, Antoine Jay, Olivier Hardouin Duparc, Jelena Sjakste, Keevin Béneut, Nathalie Vast, Yann Le Godec

- Boron carbide shows boron vacancy in the chain under non-hydrostatic torsional stress
- Chain vacancies could explain loss of mechanical strength in boron carbide during dynamic loading

Boron carbide under torsional deformation: evidence of the formation of chain vacancies in the plastic regime

Amrita Chakraborti[a,b,d], Antoine Jay[c], Olivier Hardouin Duparc[a], Jelena Sjakste[a], Keevin Béneut[b], Nathalie Vast[a], Yann Le Godec[b]

[a] *Laboratoire des Solides Irradiés, CEA/DRF/IRAMIS, École Polytechnique, CNRS, Institut Polytechnique de Paris, 91120 Palaiseau, France*
[b] *Institut de Minéralogie, de Physique des Matériaux et de Cosmochimie (IMPMC), Sorbonne Université, UMR CNRS 7590, Muséum National d'Histoire Naturelle, IRD UMR 206, 4 Place Jussieu, 75005 Paris, France*
[c] *Laboratoire d'analyse et d'architecture des systèmes, CNRS, 31031 Toulouse cédex 4, France*
[d] *Currently at Bayerisches Geoinstitut, Universität Bayreuth, Bayreuth 95440, Germany*

Abstract

We report a combined experimental and theoretical study of boron carbide under stress/deformation. A special rotating anvil press, the rotating tomography Paris Edinburgh cell (RoToPEC), has been used to apply torsional deformation to boron carbide under a pressure of 5 GPa at ambient temperature. Subsequent damages and point defects have been analysed at ambient pressure by energy dispersive X-ray microdiffraction at the synchrotron and by Raman spectroscopy, combined with calculations based on the density functional theory (DFT). We show that apart from the signals due to B_4C, new peaks appear in both characterisation methods. The DFT calculations of atomic structures and phonon frequencies enable us to attribute most of the new peaks to boron vacancies in the intericosahedral chains of boron carbide. Some of the Raman spectra also show three peaks that have been attributed to amorphous boron carbide in the literature. Deformed boron carbide thus shows small inclusions of clusters of boron carbide with chain vacancies, and/or small zones interpreted as amorphous zones.

Keywords:
boron carbide, shear stress due to torsion, non-hydrostatic stress, Rotating

Email addresses: Amrita.chakraborti@uni-bayreuth.de (Amrita Chakraborti), nathalie.vast@polytechnique.edu (Nathalie Vast), yann.le_godec@sorbonne-universite.fr (Yann Le Godec)

tomography Paris Edinburgh Cell, dynamic loading in boron carbide, chain vacancies in boron carbide

1. Introduction

The properties of boron carbides under stress/deformation have been a long-standing puzzle. On one hand, B_4C has outstanding static mechanical properties with, notably, the Vickers hardness ranging from 38 GPa up to 45 GPa in single crystals [1]. But on the other hand, its behaviour under dynamical loading is very different. Though it has the highest Hugoniot elastic limit (HEL) among ceramic materials, around 15-17 GPa [2, 3, 4], the shear strength in the shocked state rapidly decreases beyond the HEL, resulting in premature failure of the material as the shock stress reaches a threshold value of 20 GPa [5].

Several hypotheses have been put forward to explain the failure of boron carbide under dynamical loading. First, the occurrence of a phase transition has been suggested [6] including by Werheit *et al.* who have suggested a phase transition by citing changes in optical properties of the material, as well as analysing subsequent Raman peaks [7]. Vogler *et al.* have however noted that the material after the hypothetical phase transition is similar to undeformed boron carbide (figure 1(a)) [8] for dynamic loading. Moreover, in materials that show a polymorphic phase transition under shock, like sapphire [9, 10, 11] or GaAs [12, 13], the crystal-to-crystal phase transition also occurs upon reversible loading under static conditions, for instance in a diamond anvil cell [14]. However, X-ray diffraction results have not provided any evidence of a phase transition in boron carbide under reversible loading: the cell parameters decrease monotonically [15]. Therefore there is no characterisation of the hypothetical high-stress phase. The behaviour of the Raman peaks and the optical absorption under high pressure show qualitative changes that have been interpreted as the occurrence of a smooth structural modification in the motif of the boron carbide crystal structure [7, 16, 17, 18]. This suggests that hydrostatic pressure would thus modify the C-B-C chains while leaving the ($B_{11}C$) icosahedral structure intact. Werheit, however, disagrees with this argument [19] and thinks that modification of icosahedra must not be excluded, based on an analysis of the density of electronic states of some atomic configurations computed in Ref. [20].

Finally, another kind of phase transformation has been suggested: the occurrence of shear bands containing amorphous solid have been observed

under nanoindentations [21, 22], shock-wave loading experiments [23] as well as during one experiment in a diamond anvil cell, upon decompression after loading above 25 GPa [24]. The measured mechanical properties would then be strongly influenced by the amorphous zone [25, 22]. Nonetheless, the nature of the amorphous solid varies, it could be amorphous carbon or amorphous boron carbide. Its proportion is tiny with respect to the proportion of remaining boron carbide. Moreover, no clear consensus has been reached so far about the mechanisms leading to amorphisation in boron carbide nor about the interpretation of experimental and computational results [26].

Alternatively, some of us have suggested a different mechanism, *via* the formation of point defects, for the loss of mechanical strength beyond the HEL, based on density functional theory (DFT) calculations. It would result from the formation of vacancies under dynamic loading [27]. By computing the formation energy of various neutral vacancies in boron carbide, we have shown that boron atoms at the centre of the C-B-C chains are the most prone to form vacancies. The drastic consequence of the presence of such chain vacancies in boron carbide driven to the plastic regime is the formation of new carbon-carbon bonds in the chains: upon application of pressure, new C-C bonds form in the chains, leading to volume variation and ultimately, to the degradation of the material.

The intrinsic concentration of vacancies in boron carbide is too small by itself to lead to mechanical failure [24, 28]. This is compatible with the fact that undeformed boron carbide maintains large mechanical strength even under high temperature conditions [2]. However, the amount of point defects in a crystal can increase drastically under plastic deformation, due to the formation and motion of jogs for instance [29, 30, 31]. Therefore, our hypothesis is that above the Hugoniot limit, a significant concentration of vacancies appears in the ceramic and a large proportion of them undergoes the C□C to C-C transformation, where the symbol □ stands for the chain boron vacancy.

However, so far, no experimental proof of the formation of chain vacancies in deformed boron carbide has ever been reported. The purpose of the present work is thus to drive boron carbide to the plastic regime in a controlled way and to analyse the subsequent defects and damages thus formed in the material. To this end, we report a combined experimental and theoretical study. In the experiments, a special type of rotating anvil press, the rotational tomography Paris-Edinburgh cell (RoToPEC) designed by some of us, has been used to obtain non-hydrostatic torsional stress in boron carbide. The RoToPEC allows us to exercise greater control on the

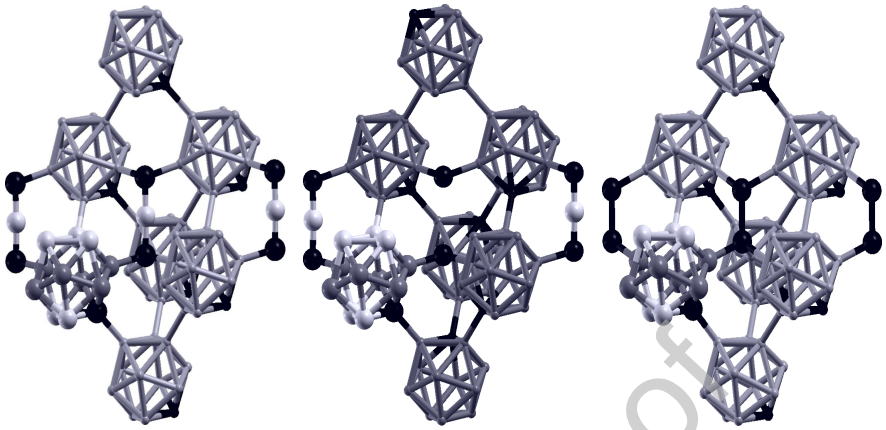

(a) $(B_{11}C)$C-B-C (b) C□C in a B_4C matrix (c) $(B_{11}C)$C-C

Figure 1: *Panel a: Atomic structure of B_4C boron carbide with ordered $(B_{11}C)$ icosahedra. Panel b: Boron vacancy isolated in one of the C-B-C chains of $(B_{11}C)$C-B-C with substitutional polar disorder. Panel c: Ordered $(B_{11}C)$C-C (Ref. [28]). The black balls represent the carbon atoms, the grey balls represent the boron atoms at equatorial sites, while the white balls represent the boron atoms at polar sites and chain centers.*

experimental parameters such as temperature and pressure conditions than conventional velocity impact experiments [8, 32]. In the theory, DFT calculations have been used to interpret the subsequent atomic structure, to search for evidence of the chain boron vacancy formation, and to check the conditions under which such C□C intericosahedral configurations might be present.

In section 2, we discuss the materials and methods used in the course of the current work. Next, in section 3 we report the experimental observations and in section 4 theoretical results are shown. Experimental and theoretical are compared and discussed in section 5. Finally, the conclusions of the work are put forward in section 6.

2. Materials and methods

2.1. Experimental method

Torsional stress has been applied to compressed boron carbide with the RoToPEC press. While the detailed mechanical description of this device can be found elsewhere (Ref. [33]), we briefly mention here that the two opposed anvils can rotate independently under load with no limitation in

the rotation angle, through two sets of gear reducers and thrust bearings located at the end of each anvil. The accurate rotation of the anvils is monitored by stepper motors and encoders, with an angular resolution of 0.02°. The working principle of the RoToPEC requires the sample chamber to be completely filled (see figure S1 of supplementary materials) and to this end, the use of powder sample was the best possible technical choice. Indeed, it is notoriously difficult to machine the very hard boron carbide material into a solid cylinder that fits for the RoToPEC. In the present case, an uniaxial pressure of 5 GPa has been applied vertically (see figure S1) in order to prevent the sliding between the powder grains [34]. The considerable inhibition of relative displacement of the grains by the pressure at room temperature is also expected to limit the shear stresses on the grains to those exerted by the torsion generated by the RoToPEC. Since boron carbide has good wear resistant properties at room temperature [35], it is improbable that there would be any significant friction inflicted structural damage in the surface of the boron carbide grains at the pressure-temperature conditions mentioned in the current work: in fact, no example of such structural change in boron carbide has been found in literature [36, 35].

Three such experiments have been performed under a pressure of about 5 GPa, with various degrees of rotation of the anvils : 90°, 180° and 270° (table 1). The pressure was determined by the value of the primary pressure on the press, which had been calibrated using *in situ* experiments at synchrotrons with pressure calibrants, similar to the calibration method for the conventional Paris-Edinburgh press [37, 38, 39]. In all of our experiments, only the lower anvil was rotated, while the upper one was kept fixed. The speed of rotation of the lower anvil was maintained at 0.01°/second. After each experiment, the pressure was released slowly over thirty minutes.

2.2. Material

Samples subjected to torsion consisted of commercial boron carbide powder (Alfa Aesar, particle size < 10 μm, 99+ % purity), that was put inside a fired pyrophyllite gasket. The powder was confined inside the gasket by using one MgO plug on each end. The gasket was then placed inside the RoToPEC and subjected to a pressure of 5 GPa at room temperature, and a torsion of a given angle at the same time. The torsion angle was precisely controlled. We note that in principle, the centre of the gasket has no torsional stress: the further the sample grain(s) are from the gasket centre, the larger the effect of the torsion.

Special attention has been given to the choice of the pressure load in order to reproduce the stress conditions generated in a shock wave experi-

Expt. name	Rotation (°)	EDXRD	Raman	Summary
RP 1	270	changes	changes	C□C clusters detected
RP 2	180	no changes	changes	no C□C configurations detected
RP 3	90	no changes	no changes	no C□C configurations detected

Table 1: *Rotation angles used for the deformation experiments done using the RoToPEC and summary of the characterisations with respect to reference B_4C.*

ment with high velocity impact as closely as possible [5]. The chosen value is based on the known value of the Hugoniot elastic limit (HEL) of boron carbide, 15-17 GPa [2, 3, 4], and on the fact that our calculations with density functional theory in the generalized gradient approximation (DFT-GGA) have shown that when boron carbide is heated to a temperature of 2000 K, the computed thermal expansion is equivalent to an internal pressure of -12.2 GPa (see e.g. Ref. [40]). Thus, whenever, in a shock wave experiment, a dynamical stress of 17 GPa (the HEL of boron carbide) is applied and the elevation of temperature is up to 2000 K [41, 42, 43], the equivalent state of stress at ambient temperature amounts to (17-12.2) GPa = 4.8 GPa [40]. Therefore, a value of 5 GPa during the generation of the torsion at ambient temperature is expected to be a good approximation of the non-hydrostatic conditions as those near the HEL for boron carbide [44].

The commercial boron carbide powder and some high purity single crystals synthesised at high temperature [45] have the composition of $B_{4.3}C$, however we use B_4C in this work as a general name for boron carbide. The XRD spectra and Raman spectra after the deformation has been compared with the spectra of the undeformed initial boron carbide powder, and the new peaks, both in XRD and Raman, are those peaks that were formed after the deformation and were absent in the initial boron carbide experimental spectra. Thus, the methodology of the attribution of the new peaks already takes into account the structural defects possibly present in the undeformed boron carbide powder.

2.3. Post-mortem sample characterisation

Samples have not been directly recovered after the pressure release. Due to the nonuniform radial deformation of the sample, it was decided to keep the sample inside the pyrophillite gasket for the post mortem characterisation. This avoids the mixing of undeformed and deformed powder and enables us to characterise the defects as a function of the radial distance.

Indeed, in principle, apart from what is induced by the (reversible) pressure load, no deformation is expected at the centre of the assembly, while

deformation maxima is expected to occur on the sample edge near the gasket. In between the centre and the edge of the sample, the deformation is expected to be a function of the radial distance, as is the torque produced τ, whose expression is $\tau = r \times F$, r being the radial distance and F is the applied force.

Two complementary characterisations have been performed: energy dispersive X-ray diffraction and Raman spectroscopy.

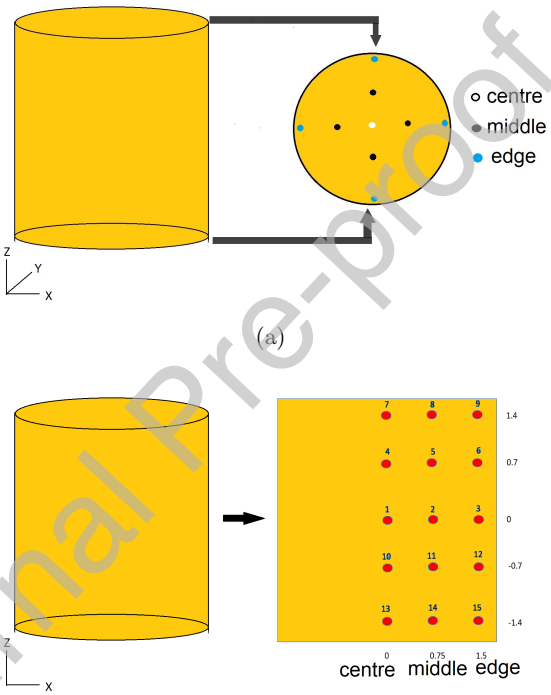

Figure 2: *(a) For one sample, the nine positions on the top and bottom of the gasket - filled with boron carbide - where Raman spectroscopy has been performed (blue, back, white circles) (b) Positions in the cylindrical space of the gasket where EDXRD has been performed (red colour). The (0,0) coordinates refer to the centre of the sample (equivalent to the gasket centre), marked with the label "1". The deformation is supposed to be minimum at the centre, while the deformation maxima are expected at z= -1.4, given by the labels "15" since only the lower anvil of the RoToPEC was rotated during the deformation experiment. Point coordinates are given in mm, with the sample/gasket centre as the origin. The rectangular shape of the sample results from the projection of the cylindrical space of the gasket filled with boron carbide, onto the xz plane.*

2.3.1. Energy dispersive X-ray diffraction

In the first step of the characterisation process, the deformed samples were observed at the PSICHE beamline in the SOLEIL synchrotron, using energy dispersive X-ray microdiffraction (EDXRD). This allowed us to characterise different points in the sample volume locally, using the powerful synchrotron radiation without the requirement of any sample recovery from the gasket. Figure 2(b) shows the locations of all of the points on a cross-sectional view of the sample volume where EDXRD has been performed. The positions were chosen assuming that the deformations in the sample would be radially symmetric.

The white beam in SOLEIL has an energy range spanning from 15 to 80 keV and it is focused to a size of 25 μm in the vertical direction and collimated to 50 μm in the horizontal direction of the sample. This limits the sample size that was scanned at each position, thus ensuring local characterisation when compared to the total sample volume (3.5 mm diameter).

The sample cross-section has been mapped using EDXRD at 15 different points of each of the three samples, leading to 45 different EDXRD patterns. Due to space constraint, only the most relevant data is shown in the next section. In the following, the EDXRD data has been converted to the corresponding peaks for Cu K-α radiation, in order to compare them with the XRD pattern of the initial undeformed boron carbide powder.

2.3.2. Raman spectroscopy

In the second step of the characterisation process, the same gaskets were prepared for the Raman spectroscopy. Each of the gasket was embedded in a cold resin made by mixing two parts by weight of acrylic KM-U and one part by weight of methyl methacrylate. The sample never came in direct contact with the resin: the resin only covered the MgO plugs and the pyrophyllite of the gasket.

The gasket embedded in the resin was then polished using a macropolishing device (MECAPOL P230), until the sample surface was exposed on both sides. The polishing was done as gently as possibly with a 120 grit sandpaper at a speed of 100 revolutions per minute.

The Raman spectroscopy was then performed on both the upper and lower exposed surfaces of the samples. Nine spectra were taken on each side of a sample, leading to 54 spectra in total for both sides of the three samples (figure 2(a)). The Raman spectroscopy was done in back-scattering geometry, using a Horiba Jobin Yvon HR800 Raman spectrometer with $\times$ 10 and $\times$ 20 objectives. The 514.5 nm line of an Ar^+ laser, with 2 μm beamspot, is used to measure the atomic vibration frequencies in the samples. Even

though work done by Werheit *et al.* [46, 47] seems to suggest the use of a higher wavelength laser for bulk Raman spectroscopy of boron carbide, we have used the standard 514.5 nm exciting laser in this work because of three reasons. Firstly and mainly, the assertion that the 514.5 nm laser does not give the bulk Raman spectroscopy is controversial [48, 49, 50, 51].The choice of the energy of the exciting laser between 2.41 eV (514 nm) to 1.58 eV does not affect the positions of the Raman lines, as shown by Xie *et al* [51]. Secondly, as Raman intensity is inversely proportional to the fourth power of wavelength, using a higher wavelength laser would require much longer exposure times to obtain comparable Raman spectra, which would lead to undesirable local heating and possible heat damage in the sample which would made difficult or even impossible to distinguish the torsional damage. Thirdly, it would be impossible to compare our results with the existing literature since the 514.5 nm laser is used in many cases for the boron carbide powder spectra [24, 21].

Similar to the EDXRD results, only a few of the most pertinent spectra have been reported in the following.

It is important to note that the EDXRD and the Raman spectroscopy have not been done on the same areas of the sample. The Raman spectroscopy has been collected on the top and bottom circular areas of the sample surfaces (figure 2(a)), as these were the only areas that could be accessed with optical means without destruction of the sample. The areas where Raman spectroscopy was performed, however, are close to the positions 7, 8, 9 and 13, 14, 15 in figure 2(b).

2.4. Computational methods

Total energy and phonon calculations have been performed within the density functional theory (DFT)) [52, 53] and density functional perturbation theory (DFPT) [54] with the pseudopotential and plane-wave method. Both the generalised gradient approximation in the PW91 parameterisation (GGA-PW91) [55] and the local density approximation (LDA) [56] have been used, the former for the characterisation of the atomic structures, energetics and calculation of the enthalpy, and the latter for the energetics and for the phonon frequencies at the centre of the Brillouin zone (BZ).

Three kinds of models have been used for the defective atomic structure, with the aim of representing either cluster of defects or isolated defects.

2.4.1. Ordered models for boron carbide

Firstly, cluster of defects have been modelled by one single crystalline phase, repeating periodically the 14- or 15-atom unit cell, to obtain the

crystal unit cells of ordered $(B_{11}C^p)C\square C$, $(B_{11}C^p)$C-C and of the reference $(B_{11}C^p)$C-B-C. The subscript ^{p} indicates that the carbon atom is in one of the six equivalent atomic positions of the polar site of the icosahedron. In such elementary unit cells, the polar carbon atom is located at the same atomic position from one cell to the other (see *e.g.* figures 1(a) and 1(c)), and the crystal symmetry is monoclinic. To obtain the XRD patterns, the base-centered monoclinic unit cell parameters and atomic positions have been averaged in the trigonal symmetry, as reported in section S3 of supplementary materials.

Phonons at zone centre have been computed for these structural models. Main approximations for the computation of vibrational properties are the Born-Oppenheimer approximation and the harmonic approximation.

From the group theory, one expects 12 Raman-active frequencies for B_4C in the $R\bar{3}m$ space group, of which seven modes have the E_g symmetry and five modes have the A_{1g} symmetry [57]. Removing the chain centre atom only affects the number of infrared active modes so that 12 Raman-active modes are also expected for $(B_{11}C^p)C\square C$ and $(B_{11}C^p)$C-C. The phonon eigenvectors of the monoclinic cells have then been projected onto the phonon eigenvectors of a crystal with the trigonal symmetry to retrieve the vibrational modes that are Raman active in the average trigonal symmetry. We choose the theoretical (B_{12})C-C-C crystal as our trigonal reference. To follow each of the Raman-active modes as closely as possible, we have designed the projection paths given below [58]:

- (B_{12})C-C-C $\rightarrow$ $(B_{12})C\square C \rightarrow (B_{11}C^p)C\square C$ for the vacancy;
- (B_{12})C-C-C $\rightarrow$ $(B_{12})C\square C \rightarrow (B_{12})$C-C $\rightarrow (B_{11}C^p)$C-C for the diatomic chain;
- (B_{12})C-C-C $\rightarrow$ (B_{12})C-B-C $\rightarrow (B_{11}C^p)$C-B-C for the reference boron carbide.

2.4.2. Models for substitutional disorder in boron carbide

Secondly, to investigate the effect of the lift of symmetry in the ordered models, and to reproduce numerically the more symmetric $R\bar{3}m$ space group observed experimentally in boron carbide, 3x3x3 supercells that contained 27 icosahedra have been constructed and the substitutional disorder of carbon atoms in the six equivalent atomic positions of the polar site of the icosahedra was reproduced (see section S4 of supplementary materials). This enables us to obtain the trigonal symmetry for all of the XRD peaks, in the sense that only a limited number of peaks have a significant intensity, the

intensity of the other ones being vanishingly small. The positions of these peaks correspond nicely to the position of the peaks of the trigonal average of the ordered structure. One exception is the (221) peak of the disordered $(B_{11}C^p)C\square C$ phases (table 2, last raw, 4^{th} column), which is consistent with the fact that $(B_{11}C^p)C\square C$ has the largest monoclinic distortion (see table S1 of supplementary materials). The higher the monoclinic deformation and the Miller indices, the larger the supercell size required in order to be close to the average trigonal symmetry. As the (221) peak does not play a significant role in the discussions of section 5, the 3x3x3 supercell is sufficient for our purpose.

2θ values of the disordered phases were then compared to symmetrically averaged values of the ordered phases. They turn out to be only slightly different from corresponding peaks of the ordered phase: the mean squared difference (MSD) between the ordered phase and the phase with polar disorder amounts to 0.036° for $(B_{11}C)C\square C$ (table 2, comparison of columns 2 and 4), to 0.024° for B_4C (columns 8 and 10) and to 0.015° for $(B_{11}C)$C-C (columns 12 and 14). The MSD is the largest for $(B_{11}C)C\square C$ and the smallest for $(B_{11}C)$C-C, B_4C MSD being inbetween, which is consistent with the fact that the monoclinic distortion is the largest for $(B_{11}C)C\square C$ and the smallest for $(B_{11}C)$C-C (see table S1 of supplementary materials). In the following, XRD experiments will be compared with either of the two results, and the quantitative comparison (mean-squared differences) will be estimated with values of calculations with polar disorder.

2.4.3. Modelling isolated defects in boron carbide

Third, isolated defects have been modelled by one single $(B_{11}C)$C-C (resp. $(B_{11}C)C\square C$) defect in a 3x3x3 matrix of B_4C. Out of the 27 chains contained in the simulation cell, 26 were C-B-C ones and the remaining icosahedral space contained one $C\square C$ configuration (resp. one C-C chain). Substitutional disorder of the carbon atom in the polar site of the icosahedra has been accounted for.

2.4.4. Computational details

The size of the plane wave basis set has been limited with a cutoff energy of 80 Ry. The BZs of the elemental unit cells have been sampled with a 12×12×12 **k**-point mesh centred at Γ, whereas the BZs of the supercells have been sampled with a 2x2x2 Monkhorst-Pack mesh [59]. Metallicity has been treated by the Methfessel-Paxton smearing with a width of 10 mRy [60]. All of the lattice parameters and atomic positions have been relaxed and the

main equilibrium properties are reported in the supplementary materials (table S1 and table S2).

Finally, our aim was also to estimate the energy barrier between the C□C and C-C configurations. Indeed, the distance between the two carbon of the chain can be seen as a reaction path to go from one phase to the other, or from one isolated defect to the other. For the ordered phases, this distance has been fixed and the enthalpy calculated while all remaining atomic positions and cell parameters were relaxed. This enabled volume relaxation along the path. For the isolated defect, we used instead the climbing image nudge elastic band method [61, 62] which enabled us to find the minimum energy path at the volume of the B_4C matrix.

3. Experimental results

3.1. Energy dispersive X-ray diffractograms

With respect to initial undeformed boron carbide (figure 3, bottom curve), several new diffraction peaks appear in the XRD patterns of the RP 1 experiment when taken on the gasket edge (position 15, upper curve).

Such peaks are absent when taken at the gasket center (position 13) or at midway between center and edge (position 14) (resp. third and second curves from top to bottom). In the latter cases, the atomic structure of boron carbide is left unchanged.

In the following, the new peaks seen on the sample edge are interpreted as the formation of clusters of defects. This set of results is consistent with the expectation that the maximum deformation should occur at the edge of the sample, at the largest distance from the gasket centre. Moreover, the deformation should also be maximum at low z (position 15 in figure 2(b)) and minimum at high z (position 9 in figure 2(b)) since only the lower anvil of the RoToPEC was rotated.

In order to demonstrate the effect of the degree of rotation on the samples, the XRD patterns on the same positions as in the RP 1 experiments are shown for the RP 2 and RP 3 experiments defined in table 1 (figure 4, resp. top and bottom panels). These patterns show no difference with respect to the distance from the centre. Hence, a minimum deformation threshold is probably needed to activate the transformation mechanism.

Two unknown peaks marked with the label "a" have appeared in all of the spectra at the 2θ values of 24.2° and 27.4°. These peaks appear whatever the torsion angle, even near the centre of the samples where the deformation induced by the torsion is negligible, as confirmed by the non variation of other peaks in this region. Hence, they are attributed to escape

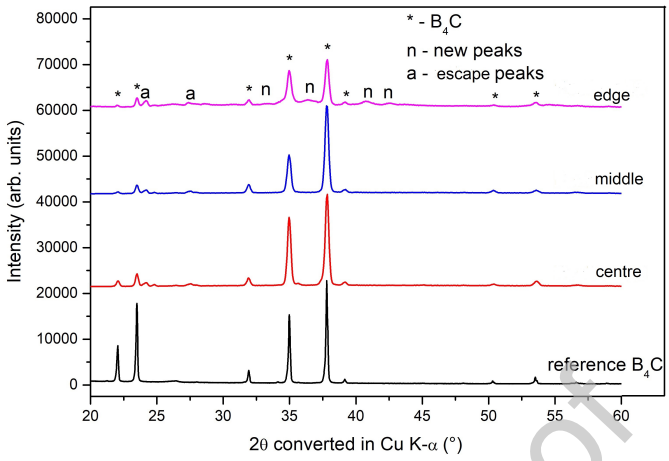

Figure 3: *Characterisation at ambient pressure of the sample from the RP 1 experiment. X-ray microdiffraction pattern of the rectangular cross-section of the gasket rotated by 270° under 5 GPa in the RoToPEC (table 1). The legends 'edge', 'middle' and 'centre' correspond to positions 15, 14 and 13 respectively (see figure 2(b)). The black line shows the XRD of the boron carbide powder at ambient pressure before deformation.*

peaks from the germanium detector, and not to a peak arising because of defects formed in the sample itself. If these peaks are excluded, four peaks are new and all of them coincide with those expected by the theory for $(B_{11}C^{p})C\square C$, as will be shown in Sec. 5 below.

3.2. Raman spectra

For the sample of the RP 1 experiment, the Raman spectra along three distinct directions of the circular surfaces also showed changes when the probing laser beam was moved from the gasket centre towards the edge (figure 5). However, the correlation between spectral changes and the radial distance at which the spectrum has been taken is not as strict as in the case of the XRD patterns. This can be seen in particular in figure 5(c), where at midway between the gasket centre and edge, the number of peaks is larger than on the edge, and the additional peaks appear to be more harmonic than the initial undeformed boron carbide peaks.

Raman spectra of the sample obtained from the RP 2 experiment show some changes (figure 6, top panel), while no changes have been observed for the RP 3 experiment for which the torsion is the smallest (panel 6(b)).

These Raman observations underscore the effect of the angle of rotation in creating deformation, and thus defects, in the sample. The larger the torsion angle, the greater the number of changes in the spectra.

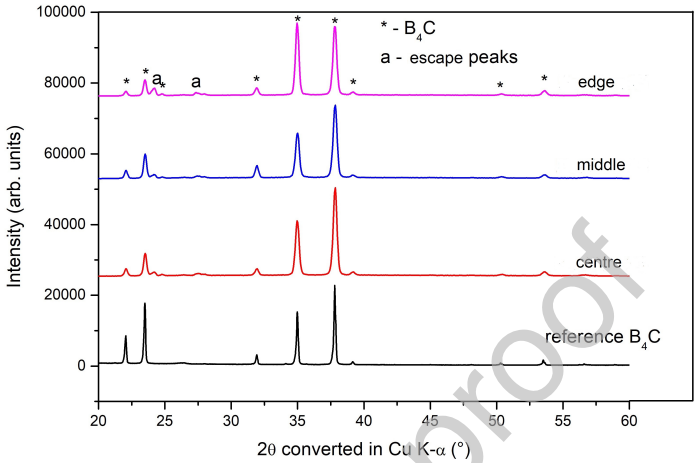

(a) EDXRD on the gasket after the RP 2 expt.

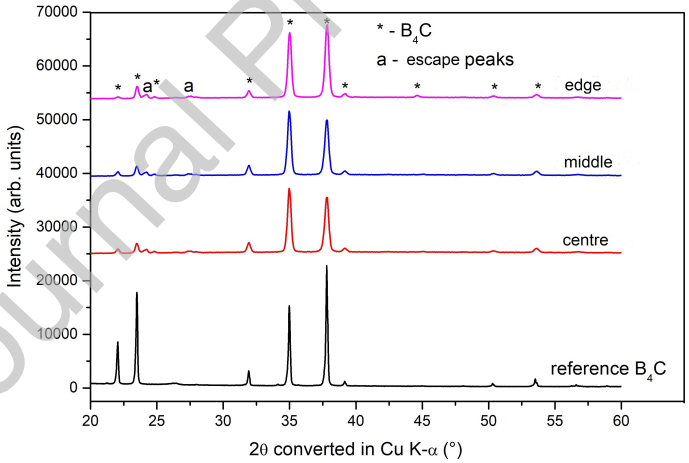

(b) EDXRD on the gasket after the RP 3 expt.

Figure 4: *X-ray microdiffraction pattern of the rectangular cross-section of the gasket rotated by resp. 180° (RP 2 experiment, top panel) and 90° (RP 1 experiment, bottom panel). Same legends as in figure 3.*

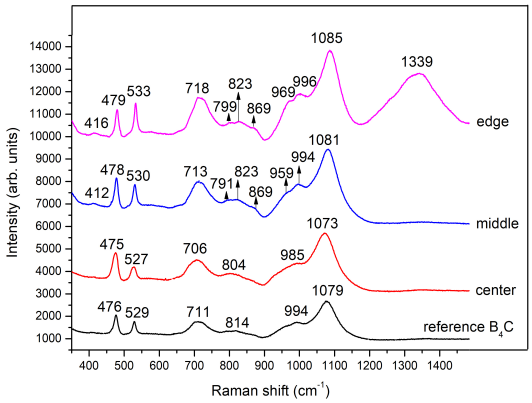

(a) Along direction 1

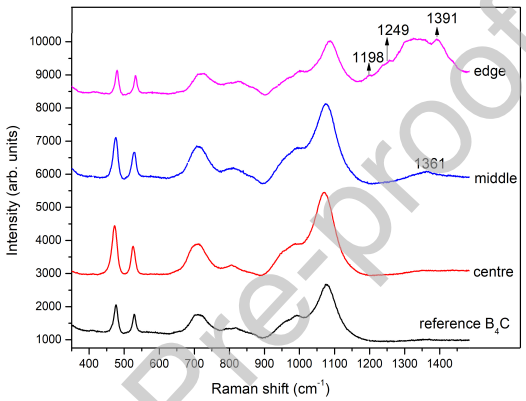

(b) Along direction 2

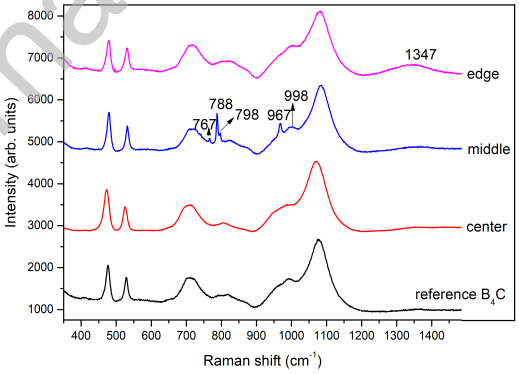

(c) Along direction 3

Figure 5: *The Raman spectra along three distinct directions of the circular sample surface rotated by 270° (RP 1 experiment). The position where the spectrum was taken has been varied from the disc-centre to the disc-edge along the radius. The black line shows the spectrum of initial undeformed boron carbide powder at ambient pressure.*

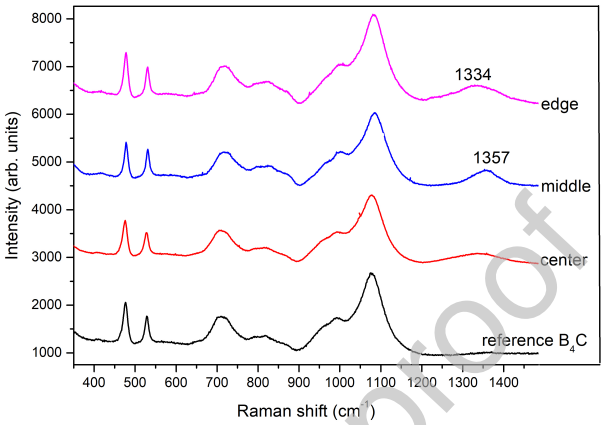

(a) The Raman spectrum after the RP 2 experiment

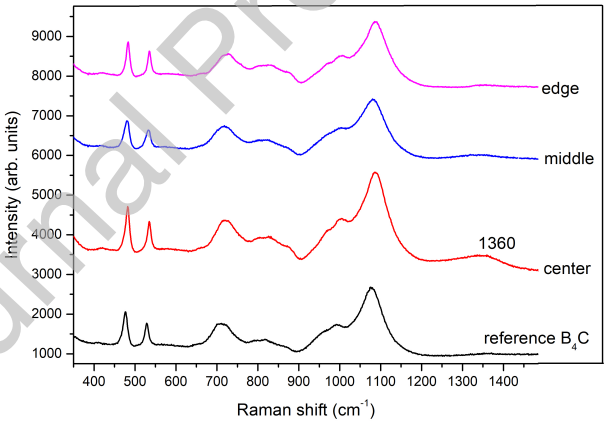

(b) The Raman spectrum after the RP 3 experiment

Figure 6: *The Raman spectra of the circular surface of the gasket rotated by resp. 180° (RP 2 experiment) and 90° (RP 3 experiment) in the RoToPEC along one direction. Same caption as in figure 5. No amorphous boron carbide signature is observed in RP 3, unlike RP 2.*

4. Theoretical results

In the following, we look for the spectroscopic fingerprints of the C□C configuration in large clusters or as a defect isolated in a matrix of B_4C (fig. 1(b)). We also study the configuration in which the C-C bond is formed and the chain is diatomic (fig. 1(c)), as this configuration with diatomic chains is expected at large pressure [27, 63]. It needs to be understood whether, in the experiments, the pressure of 5 GPa applied together with the torsional deformation is expected to lead to the C□C → C-C transformation once chain vacancies have been formed.

4.1. Formation energy

The review of the formation energy of various neutral vacancies in boron carbide shows that the boron atom vacancy at the centre of the C-B-C chains has the lowest formation energy among neutral vacancies [64, 27, 65, 48]. Its value depends on the chemical potential of boron, and ranges from 1.62 to 1.77 eV/defect for the neutral vacancy in a 2x2x2 supercell, and from 2.16 to 2.31 eV/defect for the vacancy charged with one electron (DFT-LDA, Ref. [48]). In our 3x3x3 supercell with substitutional disorder on the polar site, the DFT-LDA formation energy is slightly higher, 1.96 eV for the neutral C□C vacancy with respect to B_4C with polar disorder. For the C-C chain, it amounts to 2.73 eV. We note that the boron chain vacancy is however not the defect having the lowest energy: at low temperature, the Pandey concerted exchange mechanism between the polar carbon atom and the polar boron atom of a neighboring icosahedron leads to the *bipolar* defect complex that has the lowest energy which amounts to only one fourth of an eV in DFT-LDA [66, 64, 48].

The fact that vacancies primarily form in the chains is consistent with an earlier study that showed that the boron atom at the chain centre is weakly bonded to the atoms at the chain ends, since their shorter C-B distance, 1.43 Å (see table S1) points towards substantial π-bonding [67]. It is also confirmed by more recent calculations of isolated defects and cluster of defects [68, 27, 63, 65, 48].

This is also consistent with experiments: boron atoms at chain centres are known to have a high thermal Debye-Waller factor in X-ray diffraction data. Up to 15-25% chain centers have been observed to be boron vacancies in neutron diffraction data [69]. Moreover, the weak bonding of some of the boron atoms is also demonstrated from the fact that only boron atoms are evaporated from a heated surface of pure B_4C [70].

	C□C					B_4C matrix						C-C				
$R\bar{3}m$	Ordered		Disordered		Isolated defect		Ordered		Disordered		Ordered		Disordered		Isolated defect	
hkl	2θ (°)	*I*	2θ (°)	*I*	2θ (°)	*I*	2θ (°)	*I*	2θ (°)	*I*	2θ (°)	*I*	2θ (°)	*I*	2θ (°)	*I*
1 0 0	19.96	(46)	19.87	(7)	19.70	(13)	19.72	(8)	19.67	(12)	20.06	(17)	20.04	(32)	19.71	(12)
1 1 1	22.38	(63)	22.53	(25)	22.06	(7)	21.98	(24)	22.04	(6)	23.89	(7)	23.95	(0.1)	22.11	(6)
1 1 0	23.82	(19)	23.87	(20)	23.50	(56)	23.49	(55)	23.47	(57)	24.39	(76)	24.39	(83)	23.52	(59)
1 $\bar{1}$ 0	32.34	(2)	32.31	(7)	31.92	(21)	31.97	(11)	31.87	(31)	32.16	(4)	32.11	(11)	31.92	(20)
2 1 1	35.47	(116)	35.64	(116)	34.97	(72)	34.89	(61)	34.93	(69)	37.20	(77)	37.25	(82)	35.03	(71)
1 $\bar{1}$ 1	38.30	(**100**)	38.27	(**100**)	37.79	(**100**)	37.84	(**100**)	37.73	(**100**)	38.19	(**100**)	38.14	(**100**)	37.79	(**100**)
2 1 0	39.68	($\approx$ 0)	39.75	(0.2)	39.14	(2)	39.14	(5)	39.08	(2)	40.46	(12)	40.45	(8)	39.17	(3)
2 0 0	40.56	(4)	40.56	(0.2)	40.03	(0.8)	40.05	($\approx$ 0)	39.95	(0.9)	40.77	(1)	40.73	(0.8)	40.03	(0.9)
2 2 1	42.34	(1)	42.20;42.57	(0.2;0.3)	41.73	(0.2)	41.62	($\approx$ 0)	41.68	(0.2)	44.69	(2)	44.77	(0.4)	41.82	(0.2)

Table 2: *XRD theoretical peaks of the ($B_{11}C^p$)C□C and ($B_{11}C^p$)C-C configurations, in the periodically repeated 14-atom ordered elemental unit-cell (columns: 2-3,12-13); in a 378-atom 3x3x3 supercell with substitutional disorder in the polar site of the icosahedra (columns: 4-5,14-15); as an isolated defects in a 404-atom 3x3x3 supercell of B_4C^p with polar substitutional disorder (columns: 6-7, 16-17). Peaks of pristine phases are also understood as those of clusters of defects (columns 2-5 and 12-15). Peaks of the B_4C^p matrix are given for reference, either for the 15-atom ordered phase (columns: 8-9) or for the phase with polar substitutional disorder (columns: 10-11). 2θ values are given in Cu K-α. Peak intensities have been normalised to the (1 $\bar{1}$ 1) peak of each phase. Small peaks ($I < 4.5$) occurring in supercells below 19.56° are not shown. High 2θ values have not been observed in present experiments, theoretical ones can be found in table B.13 of Ref. [58] for the ordered phases.*

4.2. Atomic structures

In the absence of the boron atom, the chain evolves from the triatomic (C-B-C chains) to the C□C configuration, with a drastic change of the first-neighbour distance in the chain d_{chain}. Consequent spectroscopic fingerprints of this change can been seen in the theoretical XRD peaks (table 2) and depend on whether the defect is isolated in a matrix of B_4C (columns 6-7) with $d_{chain} = 3.05$ Å, or whether a large number of neighbouring defects are formed (columns 2-5) with $d_{chain} \approx 2.86$ Å.

For an isolated defect, the peak positions are shifted towards slightly higher values than in B_4C, with a mean squared shift (MSS) of the nine 2 θ values of 0.017°. The shift is larger for the C-C defect, the MSS reaching 0.027°. The peak positions are merely shifted towards slightly higher values of 2 θ, which reflects a slight crystal volume decrease that is larger for the C-C defect than for the C□C defect. The diffraction pattern is similar to that of pristine B_4C and the occurrence of isolated defects cannot explain the new peaks observed in the experiments. The 2 θ values of isolated defects are very close to those of B_4C which indicates that isolated defects, if any, cannot be detected by EDXRD.

For clustering defects on the contrary, the average theoretical MSS shift of $(B_{11}C^p)$C□C, taken as a crystal, with respect to undeformed $(B_{11}C^p)$C-B-C, is one order of magnitude larger than that of the isolated defect and amounts to 0.184° (columns 4 and 10). The intensities also show some changes (columns 5 and 11), as in particular the relative intensities of the two most intense peaks are modified (*hkl* peaks 2 1 1 and 1 $\bar{1}$ 1).

Changes are more important when chains evolve from triatomic to diatomic (C-C chains) than to C□C configurations, with a MSS as large as 0.524° (columns 10 and 14).

Remarkably, all of the new peaks observed in EDXRD characterisations after large deformation coincide well with the peaks of the $(B_{11}C^p)$C□C, as discussed in section 5.

4.3. Behaviour of the chain vacancy under pressure

In this section, we study the effect of pressure on the chain vacancy, as in our experiment, a pressure of 5 GPa is applied simultaneously with the torsional deformation. The question that arose was whether this pressure would be sufficient to modify the vacancy configuration so that a new C-C bond is formed. To this end, we present the enthalpy as a function of the relative distance between the two carbon atoms of the chain for various pressure values (figure 7).

In fact, the presence of a vacancy in the chain leads to the presence of dangling bonds between the carbon atoms [63], and to defect-induced energy levels in the band gap of the Kohn-Sham electronic band structure. Such a defective electronic configuration tends to be restabilised, either, at ambient pressure, by capturing a charge [58, 65, 48], or, as previously studied [27, 63], by forming a carbon-carbon bond under pressure (figure 7).

As far as energy at both ambient pressure and thermodynamical equilibrium is concerned, a crystal in which all of the intericosahedral spaces contain C-C chains is competing with the crystal in which they all contain C□C configurations (figure 7, left panel, dashed line). The energy difference at ambient pressure between the $(B_{11}C^p)$C□C and $(B_{11}C^p)$C-C phases is smaller than 100 meV, and it is hard to decide from our calculations which one is the most stable phase: $(B_{11}C^p)$C□C is the most stable phase in DFT-GGA-PW91, while $(B_{11}C^p)$C-C is the most stable one in LDA (not shown).

At thermodynamical equilibrium the two structures can coexist, and which one of the phase is formed depends on the conditions of formation. The two phases are however separated by an energy barrier of 0.33 eV at zero pressure, so that once vacancies are formed, the probability of formation of C-C bonds is negligible unless one of the physical variables is modified: for instance, application of an hydrostatic pressure lowers the energy barrier. At 6 GPa, the energy barrier is 0.21 eV (figure 7, left panel). Ultimately, at approximatively 28 GPa in the DFT-GGA-PW91 calculations -and 20 GPa in DFT-LDA [63]- only the $(B_{11}C^p)$C-C phase can exist. This (hydrostatic) pressure is larger than the expected uniaxial pressure reached in our experiments.

When the defect is isolated in a matrix of B_4C, for steric reasons, the energetic competition turns out to be in favour of the C□C configuration (figure 7, right panel, dashed line). The volume of $(B_{11}C^p)$C□C is smaller then the volume of B_4C, the volume of $(B_{11}C^p)$C-C being even smaller [28] (see table S1 for the volumes of the ordered phases). The presence of the B_4C matrix constrains the C□C configuration in extension and the C-C chain in even larger extension. The presence of the B_4C matrix thus stabilises the C□C configuration, by 0.6 eV at ambient pressure (figure 7, right panel, dashed line). The energy barrier amounts to 0.46 eV at 5 GPa and to 0.35 eV at 10 GPa, so that only under pressures higher than 28 GPa (not shown) does the isolated C-C bond replace the vacancy.

In conclusion of this section, the formation of a C-C bond, replacing a vacancy, is not expected under a moderate value of the hydrostatic pressure. The case of an uniaxial pressure led to similar conclusions for clusters of

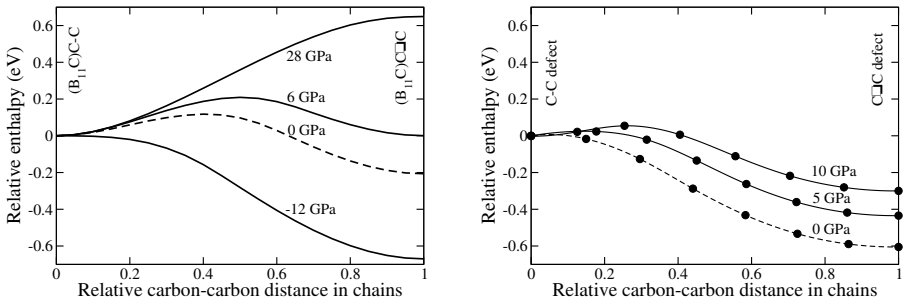

(a) Defect cluster (b) Isolated defect

Figure 7: *Theoretical energy barrier between the C□C and C-C configurations of the chain. Left panel: in the periodically-repeated 14-atom unit cell, at zero pressure (dashed line), in compression up to 28 GPa, and in extension down to a negative pressure of -12 GPa (solid lines). Volume relaxation was accounted for along the path. Right panel: isolated chain-defect in a 3x3x3 matrix of ordered B_4C at ambient pressure (dashed line) and in compression up to 10 GPa (solid lines), computed with the nudge elastic band method at the volume of the B_4C matrix for a given pressure. Computations in DFT-GGA-PW91.*

defects [63]. Whenever C-C bonds are formed in the experiments, this would be attributed to the unusual conditions in the RotoPEC, where both uniaxial pressure and torsional deformations are applied.

4.4. Vibrational properties

The Raman-active vibrational frequencies are reported for the ordered $(B_{11}C^p)$C-B-C (table 4), $(B_{11}C^p)$C□C and $(B_{11}C^p)$C-C phases (table 5).

Going from C-B-C to C-C and to C□C configurations in the intericosahedral space induces changes in all of the vibrational frequencies. The main change, however, is for the symmetric stretching mode of the chain (cs) that we have called $Ch5$. Its frequency goes from 1095 cm^{-1} to 570 cm^{-1} (in the case of C-C) and 398 cm^{-1} (in the case of C□C). This evolution comes from the distance between the chain atoms, which increases from 1.42 Å to 1.73 Å and to 2.84 Å in DFT-LDA (and from 1.43 Å to 1.80 Å and to 2.92 Å in DFT-GGA), see table S2 (resp. table S1).

The libration of the icosahedra has similar frequencies in all of the materials ($Ico5$ also called *lib* mode) and is present in all of the experiments, which testifies to the presence of icosahedra (resp. 536 cm^{-1}, 481 cm^{-1} and 491 cm^{-1} in B_4C, $(B_{11}C^p)$C□C and $(B_{11}C^p)$C-C phases).

Finally, the (pseudo) chain rotation ($Ico7$ or pcr) is one of the characteristic Raman peaks of B_4C, together with the librational mode. It is found

at 488 cm^{-1} and 529 cm^{-1} in B_4C and $(B_{11}C^p)C\square C$, and is blue shifted by 140 cm^{-1} between B_4C and $(B_{11}C^p)$C-C, where it is at 621 cm^{-1}.

5. Discussions

Both the XRD patterns and Raman spectroscopy of the RP 1 sample show the formation of new peaks. These peaks can be explained by the formation of vacancies in the crystal structure of boron carbide due to the torsional stress generated by the RoToPEC, as we are going to show. In order to verify this hypothesis, the changes in the spectra have been compared with the spectra of the various defective boron carbides calculated in section 4. The XRD patterns are discussed in section 5.1 and Raman spectra in section 5.2. In both kinds of experimental characterisation, we identify the presence of point defects (sections 5.1 and 5.2.1). Amorphous zones have been identified by Raman scattering only (section 5.2.2). Thus, we show that EDXRD and Raman spectroscopy turn out to be complementary and mandatory in characterising the damage formed in the vicinity of the plastic deformation in boron carbide.

5.1. Comparison of experimental and theoretical XRD spectra

All of the four peaks that appear in EDXRD spectra can be explained by the theoretical calculations as coming from the formation of large clusters of unit cells with a boron chain vacancy (table 2). The formation of vacancies occurs on distances large enough to be detected by the (very accurate) EDXRD. The reason behind this cluster formation is attributed to the torsion generated in the RoToPEC.

The two most intense peaks are observed at resp. 37.73° and 34.94° (see section S5 of supplementary materials). They are attributed to B_4C and, remarkably, these two peaks are also predicted to be the most intense ones by the theoretical calculations for B_4C (column 11 of table 2). They come from the $(1\,\bar{1}\,1)$ and $(2\,1\,1)$ planes in the trigonal representation of the $R\bar{3}m$ space group.

The $(2\,1\,1)$ peak is computed at 34.93° for B_4C and at 35.64° for $(B_{11}C^p)C\square C$. These two peaks are theoretically well separated and can indeed be distinguished in the experiments (table 3). On the contrary, the $(1\,\bar{1}\,1)$ peak is the most intense peak for B_4C and the second most intense peak for $(B_{11}C^p)C\square C$, and are close to each other, at resp. 37.73° and 38.27°. Only one peak can be seen in the experiment at 37.73°.

Among the new peaks that appear upon large deformation, two can only be explained by the presence of $(B_{11}C^p)C\square C$: they come from the $(1\bar{1}0)$ and (211) planes, and are observed at resp. 33.35° and 36.29°.

Trigonal	EDXRD $2\theta(^\circ)$		Theory $2\theta(^\circ)$			Hexagonal
hkl	New	Common	C□C	B_4C	C-C	*hkl*
100			19.87	19.67	20.04	101
111		22.04	22.53	22.04	23.95	003
110		23.47	23.87	23.47	24.39	012
$1\bar{1}0$		31.91	-	31.87	32.11	110
$1\bar{1}0$	33.35		32.31	-		110
211		34.94	-	34.93		104
211	36.29		35.64	-	37.25	104
$1\bar{1}1$		37.73	38.27	37.73	38.14	021
210		39.15	39.75	39.08	40.45	113
200	40.75		40.56	39.95	40.73	202
221	42.51		42.20;42.57	41.68	44.77	015

Table 3: *XRD experimental and theoretical peak positions. 2θ values are given in Cu K-α. New peaks that have appeared in the RP 1 experiment at the edge (position 15) (figure 3) and corresponding Miller indices in the trigonal representation of the $R\bar{3}m$ (# 166) space group; Peaks common to the RP 1 expt. and to undeformed B_4C observed at the centre of the sample of the RP 1 expt.; Theoretical peaks for $(B_{11}C^p)C\square C$, B_4C and $(B_{11}C^p)C$-C in the 3x3x3 supercell with substitutional disorder of the carbon atom in the polar site.*

The other two new peaks at 40.75° and 42.51° turn out to be in better agreement for $(B_{11}C^p)C\square C$ than for B_4C, with computed angles of 40.56° and 42.20° or 42.75° (rather than 39.95° and 41.68° for B_4C).

Finally among the nine lowest $(h\,k\,l)$ planes predicted by theory, eight are observed for $(B_{11}C^p)C\square C$ and B_4C, the exception being the lowest (1 0 0) plane, which is quasi-absent from our energy-dispersive XRD experiments. The (1 0 0) plane has been observed in conventional X-ray diffraction that we performed in the laboratory on undeformed boron carbide. Its quasi-absence in EDXRD is due to to the beam profile at Soleil synchrotron, which prevents correct intensity observations at small energies (converted to small scattering angles in our results) as well as at large ones.

To quantitatively assess the assignment of the four new peaks, the mean squared error (MSE) of all of the eight peaks observed at the position 15 of RP 1 that can be corroborated with the peaks of $(B_{11}C^p)C\square C$ in table 3

has been calculated as

$$MSE = \frac{1}{8}\sqrt{\sum_i (2\theta^{expt} - 2\theta^{theory})^2} \quad (1)$$

The MSE amounts to 0.20°, for the eight peaks that could correspond to theoretical (undeformed) ($B_{11}C^p$)C□C at ambient pressure (column 4). Similarly, the mean squared error is 0.15° for the eight peaks that can correspond to the theoretical (undeformed) ($B_{11}C^p$)C-B-C (theoretical B_4C) at ambient pressure (column 6). Both MSEs are on the same order of magnitude, showing that theory yields similar accuracy w.r.t. experiment for ($B_{11}C^p$)C-B-C and ($B_{11}C^p$)C□C. We find it to be a strong argument in favour of the presence of ($B_{11}C^p$)C□C in addition to B_4C, as the presence of B_4C alone is not able to explain all of the observed peaks.

Finally, the EDXRD spectra for RP 2 and RP 3 do not show much change w.r.t. B_4C, and this observation underscores the effect of the degree of rotation on the defects formed in the sample - RP 2 (180°) and RP 3 (90°) are less deformed compared to RP 1(270°). The deformation threshold corresponds to approximately 180° of anvil rotation.

In conclusion, the comparison of EDXRD spectra between theory and experiments leads us to characterise the sample after the largest deformation as multizone, with zones of B_4C and zones of ($B_{11}C^p$)C□C, the latter of size smaller than 10 μm.

5.2. Comparison of the Raman active frequencies

The Raman spectrum of distorted B_4C is similar to that of the undeformed one (table 4, columns 2 and 3), and in agreement with the theoretical spectrum (column 4), with the provision that only 8 peaks are singled out in the experiments, as in previous works [57, 58, 48] instead of the expected 12 modes. The torsion shifts the peak positions by a few wavenumbers/cm^{-1}.

There are however a number of new peaks which cannot be explained by the presence of B_4C only and that we now discuss. They are of two types: peaks attributed to points defects, which turn out to be consistent with the XRD findings of the previous section; and those attributed to amorphous zones that cannot be detected by EDXRD. The amorphous zones could not be detected by EDXRD because of their lack of long range order: even the very wide amorphous halos due to diffused scattering that might form was not visible in presence of the sharp crystalline boron carbide peaks. Thus, EDXRD and Raman spectroscopy complement each other to characterise the damage in B_4C.

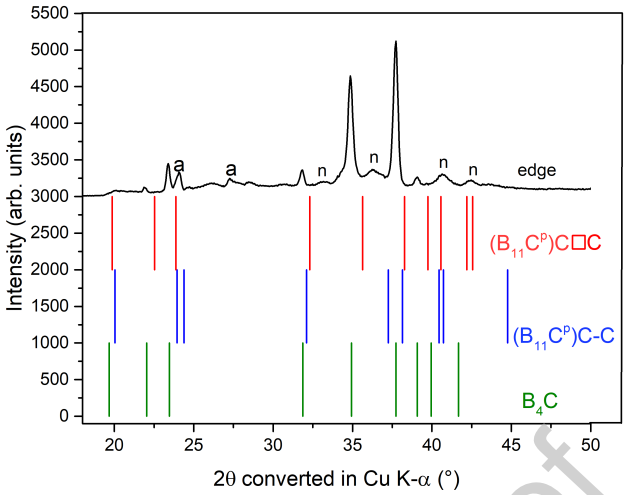

(a) EDXRD on the gasket after the RP 1 expt.

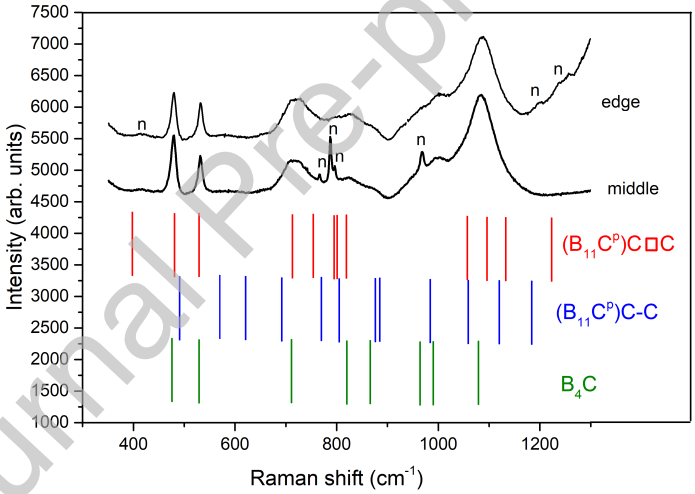

(b) Raman spectroscopy on the gasket after the RP 1 expt.

Figure 8: *(a) Experimental EDXRD pattern from RP1 (edge) and theoretical XRD peak positions for Cu K-α for undeformed $(B_{11}C^p)C\square C$ and $(B_{11}C^p)C$-C at ambient pressure and also those of the reference boron carbide powder, (b) Experimental Raman spectrum and theoretical Raman-active frequencies. Same spectrum as in figure 5(b) (edge) and figure 5(c) (middle position) of RP1 experiment. Theoretical frequencies are shown for undeformed $(B_{11}C^p)C\square C$ and $(B_{11}C^p)C$-C at ambient pressure and also those of the reference boron carbide powder.*

Raman peaks		Undeformed B_4C		Mode description	
New	Common	Reference	Theory	Name	Symmetry
416					
	479	476	479-**488**	$Ico7, pcr$	E_g
	531	529	**536**-549	$Ico5, lib$	E_g
			699	$Ico17$	A_{1g}
	717	711	**719**	$Ico9$	A_{1g}
767		-	737-**768**	$Ico11$	E_g
788		-			
798		-			
			808-815	$Ico20$	E_g
	823	820	840-841	$Ico13$	E_g
	871	866	-		
967*	967	964	-		
	998	990	994	$Ico21$	A_{1g}
			1052-1052	$Ico23, asis$	E_g
			1069	$Ico24, sis$	A_{1g}
	1082	1079	**1095**	$Ch5, cs$	A_{1g}
			1098-**1139**	$Ch3, cr$	E_g
1198					
1249					
1391					

Table 4: *Experimental and theoretical Raman-active frequencies (RAF, cm^{-1}): new peaks that have appeared in the RP 1 experiment, RAF common to RP 1 expt. and to distorted boron carbide, RAF of undeformed boron carbide at ambient pressure as observed (column 3) and computed (column 4). The Cm monoclinic symmetry in the calculations slightly lifts the degeneracy of the E_g modes. All of the peaks of reference B_4C are present in the deformed sample. The '*' signifies a much sharper peak at the frequency than the one observed for reference B_4C. pcr, lib, asis, sis, cs and cr stand respectively for the pseudo-chain rotation, libration of the icosahedra, anti-symmetric and symmetric intericosahedral stretching, symmetric chain stretching and chain rotation modes. Theoretical frequencies in bold font are expected to be the most intense ones.*

5.2.1. Point defects

In the RP 1 experiment, one new small peak is observed at 416 cm^{-1} or 412 cm^{-1} (figure 5(a)), which corresponds nicely to the $Ch5$ chain stretching (cs) mode of the $(B_{11}C^p)C\square C$ phase. This is an important finding, as the $Ch5$ mode is expected to be the most intense mode of $(B_{11}C^p)C\square C$ (figure 8(b)).

Three additional peaks are also observed at resp. 1198, 1249 and 1391 cm^{-1} (figure 5(b)). The peaks at 1198 and 1249 cm^{-1} correspond well with the peak at 1218 cm^{-1} of the $(B_{11}C^p)C\square C$ phase, and with the mode at 1184 cm^{-1} of the $(B_{11}C^p)$C-C phase. However, there has not been any corresponding peaks identified for the last peak at 1391 cm^{-1}.

Raman peaks		Theory		Mode description	
New	Common	$(B_{11}C^p)C\square C$	$(B_{11}C^p)$C-C	Name	Sym.
416		**398**	570	$Ch5, cs$	A_{1g}
	479	481-488	410-491	$Ico5, lib$	E_g
	531	529-533	592-621	$Ico7, pcr$	E_g
	717	713	692	$Ico17$	A_{1g}
			692-708	$Ico13$	E_g
				$Ico11$	E_g
				$Ico9$	A_{1g}
767		730-754	726-770	$Ico11$	E_g
788		795	805	$Ico9$	A_{1g}
798		801-827		$Ico20$	E_g
	823	819-831		$Ico13$	E_g
	871		876-918	$Ico20$	E_g
				$Ico23$	E_g
967*	967		984	$Ico21$	A_{1g}
	998			$Ico21$	A_{1g}
			1048-1059	$Ch3, cr$	E_g
		1057		$Ico21$	A_{1g}
	1082	1096-1108		$Ico23, asis$	E_g
				$Ico24, sis$	A_{1g}
1198		1133	1120	$Ico24, sis$	A_{1g}
			885-**1184**	$Ico23, asis$	E_g
1249		1218-1223		$Ch3, cr$	E_g

Table 5: *Same experimental data as in table 4, and theoretical Raman-active frequencies (cm^{-1}) of undeformed $(B_{11}C^p)C\square C$ and $(B_{11}C^p)$C-C corresponding to some of the new peaks. The Cm monoclinic symmetry of the former two lifts the degeneracy of the E_g modes. Theoretical frequencies in bold font are expected to be the most intense peak for $(B_{11}C^p)C\square C$ and $(B_{11}C^p)$C-C.*

Quite a few new peaks have also appeared at 767, 788, 798, and 967 cm^{-1} in figure 5(c) (middle position). Some of them could be matched to different predicted peaks of $(B_{11}C^p)C\square C$, as shown in figure 8(b). In fact, it is

observed from tables 4 and 5 that the entire spectra observed at this middle position could either be explained by peaks of the reference B_4C or by the peaks of $(B_{11}C^p)C\square C$, which points to the formation of small zones, of size smaller than 2 μm, of $(B_{11}C^p)C\square C$.

However, the peaks corresponding to $(B_{11}C^p)C\square C$ that have been noted in figure 5(b) have not appeared in the spectrum of figure 5(c). Moreover, the peak at 967 cm^{-1} is much sharper than the hump observed in the reference B_4C around the same frequency. Since this peak does not correspond to any of the $(B_{11}C^p)C\square C$ peaks as well, it might be the case that some other polymorph like $(B_{11}C^p)$C-C might also be present. Table 5 shows this possibility of the formation of C-C chains in the sample. This is possible if the $C\square C$ intericosahedral configurations that had been previously formed under torsion collapsed under the combined torsional and uniaxial deformation to form the C-C chains, as discussed in section 4.3.

The mean square difference between theory and experiment amounts to 5 cm^{-1} for B_4C which is remarkable given the fact calculations are limited to the harmonic approximation (table 4). It reaches 7 cm^{-1} for $(B_{11}C^p)C\square C$ when 11 modes are compared, and 13 cm^{-1} when only the six new modes at resp. 416, 767, 788, 798, 1198, and 1249 cm^{-1} are compared. The MSD for $(B_{11}C^p)$C-C amounts respectively to 15 cm^{-1} when 10 modes are compared, and to 19 cm^{-1} when only the six new modes at resp. 416, 767, 798, 967, 1198 and 1249 cm^{-1} are compared.

The boron atom displaced from the chain is expected to be placed in interstitial positions. Some of us have proposed that boron-rich boron carbide contain boron atoms in the intericosahedral space, in the *2c* and/or *6g* Wyckoff sites of the average $R\bar{3}m$ trigonal unit cell [40]. Indeed, such atomic configurations combined to (B_{12}) icosahedra and C-B-C chains forming 414 elementary unit-cells, turn out to have, in the calculations, the lowest formation energy at 8.7 and 13.0 % at. C concentrations. In the present work however, a change in the icosahedron composition could not be detected either in XRD or in Raman spectroscopy.

Finally, in the spectra shown for RP 2 in figure 6(a), there has been no new peaks corresponding to another polymorph of boron carbide, and the spectra obtained for RP 3 in figure 6(b) have shown no changes with respect to undeformed boron carbide.

5.2.2. Amorphous zones

Another important change is the occurrence, in some of our Raman spectra, of large bands that we tentatively attribute to amorphous zones.

As explained in the introduction, no clear consensus has been reached

so far about the mechanisms leading to amorphisation in boron carbide or about the interpretation of experimental or computational results [26]. Moreover, the kind of amorphous boron carbide obtained in shear bands generated in shock-wave and nanoindentation experiments [23, 24, 25, 21, 22] has to be differentiated from the amorphous boron carbide films obtained by chemical vapor deposition (CVD) [71, 72] and by irradiation [73, 74, 75].

In the former, shear bands are associated with two bands centered respectively at 1330 and 1520 cm^{-1}, and a small peak at 1810 cm^{-1}. The first two peaks have been attributed to the D and G bands of amorphous carbon, expected respectively at 1350 and 1580 cm^{-1} [25, 22], or to a kind of amorphous boron carbide [76, 24, 21]. The origin of the peak at 1810 cm^{-1} is not known. DFT calculations cannot explain the occurrence of these peaks unless pressures larger than 60 GPa are achieved [26]. These shear bands do not occur in nanoindentation experiments when a uniaxial compression smaller than 8 GPa is imposed [25], which is far enough from the value applied in the RoToPEC experiments. Awasthi *et al.* [76] have suggested that the amorphisation occurs due to melting and recrystallisation as an impact of stresses, based on multi-scale quantum mechanical and molecular dynamics modelling.

In the products synthesised by CVD, besides the D and G bands of amorphous carbon, two large Raman bands are observed at 400-700 cm^{-1} and 850-1350 cm^{-1} centered at 1050 cm^{-1} [71, 72]. The overall stoichiometry, including free carbon, was $B_{2.5}C$. Transmission electron microscopy and Raman experiments were conducted in boron carbide irradiated with slow heavy Au ions. It was shown that local arrangements are disturbed and Raman peaks become broad, similar to the CVD experiments. At high fluences, additional broad bands beyond 1200 cm^{-1} were attributed to C–C bonds [73]. In the non implanted damaged zones, only partial disorder was produced, with nanometric amorphous zones in a still crystalline matrix. It was concluded that the local damage cannot trigger complete structural disorder in the zones with no Au-implentation [73, 75].

Turning back to our result, a large peak can be seen at 1339 cm^{-1} for instance in figure 5(a), taken on the sample of the RP 1 experiment. The two other signatures at 1580 cm^{-1} and 1810 cm^{-1} were also present (not shown). We thus tentatively assign these peaks to what is called amorphous boron carbide, as mentioned in the literature about shear bands.

It is notable that in the present case, the peak that would correspond to amorphous boron carbide has an intensity similar to those of the crystalline boron carbide peaks. In fact, in none of the Raman spectra obtained so far has the amorphous boron carbide peak been more intense than the crys-

talline boron carbide peaks. Since the laser beam spot of the micro-Raman spectrometer used in these analyses is around 2 μm, we can safely conclude that the amorphous zones are very localised with areas much smaller than 2 μm. This is in accordance with what has been reported by Chen *et al.* [23] in that the bands attributed to amorphous zones, when present, are extremely localised.

Figure 5(b) has been obtained in another direction along the radius of one of the circular faces of RP 1. A small peak is observed around 1360 cm^{-1} for the spectra taken at the middle of the sample along the radius. This can be attributed to amorphous carbon or graphite (1350 cm^{-1}) [77]. This is not unusual as commercial boron carbide is known to contain a certain amount of free carbon in the samples [74]. The latter was however not detected in large quantity in undeformed boron carbide. Further investigation is required to understand whether the *D* band also comes from the deformation process in the RotoPEC. Figure 5(c) has been obtained in yet another direction on the RP 1 sample surface and we observe only a small peak that we tentatively attribute to amorphous boron carbide on the edge, with the caveat given above.

Finally, in the spectra shown for RP 2 in figure 6(a), one can notice the presence of only a feeble peak attributed to amorphous boron carbide on the edge of the sample.

5.2.3. Conclusion about Raman spectroscopy

In conclusion, the comparison of the experimental and theoretical Raman spectra leads us to characterise the sample after the largest deformation as multizone. Apart from B_4C in our samples, we also find zones of amorphous boron carbides and/or amorphous carbon, whose size is less than 2 μm, as well as zones of $(B_{11}C^p)C\square C$ of size less than 2 μm. We raised the possibility of zones of $(B_{11}C^p)$C-C. The deformation threshold for the occurrence of damage is approximately 180° of anvil rotation, and is detected to be smaller by Raman spectroscopy than by EDXRD.

We also have to consider that a vast variety of atomic configurations for boron carbide may exist due to the complexity of the system, as hypothesised by several authors [78, 79, 5]. However, energetics consideration allows us to disregard most of the high energy configurations, as the present experiments have been performed at room temperature, which hinders the overcoming of large energy barriers between two atomic configurations. In particular, it must be noted that Fanchini *et al.* [3] have suggested, based on density functional theory calculations, that shock amorphisation of the (B_{12})C-C-C polytype of boron carbide through the segregation of B_{12} icosa-

hedra and amorphous carbon is the reason for the possible source of failure of boron carbide above the HEL. However, for this hypothesis to be effective, the (B_{12})C-C-C atomic configuration should be present abundantly in boron carbide. But both DFT calculations [63, 27] and molecular dynamic simulations [80] have established that it is not the case and that (B_{12})C-C-C is not an abundant atomic configuration in boron carbide. Furthermore, detailed examination of our computed XRD pattern for (B_{12})C-C-C (not shown) indicates that this atomic configuration is not able to explain the occurrence of the new peaks at 33.35° and 36.29°. In addition, the MSE for the six common peaks is one order of magnitude larger for (B_{12})C-C-C than for B_4C. In this respect, our experimental results consisting of both Raman spectra and XRD peaks -with mean squared error of the $(B_{11}C)$CC peak being of the same order of magnitude as boron carbide itself- is a well-rounded demonstration of the presence of the $(B_{11}C)$C□C atomic configuration.

6. Conclusions and perspectives

The EDXRD and Raman spectroscopy have clearly provided evidence that chain vacancies are produced in boron carbide under the non-hydrostatic torsional stress generated in the RoToPEC, as predicted by Raucoules *et al.* [27]. In fact, this is the first experimental demonstration of chain vacancies forming in boron carbide under non-hydrostatic stress, which can lead to the well-known mechanical failure of boron carbide beyond its Hugoniot elastic limit. The samples thus appear as multizone, remaining principally B_4C with inclusions of $(B_{11}C^p)$C□C zones and/or amorphous zones. The possible presence of other polytypes of boron carbide like $(B_{11}C^p)$C-C has also been discussed. Thus, the present work offers a new solution to the long-standing puzzle of the loss of mechanical strength of boron carbide under dynamic loading.

It also opens the door to several new avenues of further investigation. Both the deformation generated and the defect concentrations can be quantified by repeating the same experiments with a wire inserted at different locations of the sample and noting the deformation of the wire using synchrotron X-ray radiography. Indeed, it is evident from the results that the defects formed depend greatly on the degree of rotation of the gasket, and a quantification of the deformation would also be valuable for further theoretical investigations.

Obtaining an absolute value of the quantity of defects is a difficult task, and a realistic aim could be to study the defect concentration change as a function of the deformation, with respect to a carefully chosen reference

state. The question of the determination of the complicated stress gradient with respect to the radial distance is a possible topic for further investigations in *in situ* experiments in synchrotron facilities. The experiments discussed in this work have been performed at room temperature. That would not result in achieving the HEL in boron carbides, and therefore would not cause any mechanical failure in the samples. However, this will bring boron carbide into the plastic regime, and produce defects and vacancies similar to those produced in boron carbides as it approaches the HEL, thus giving an opportunity to study these defects in a controlled and systematic manner. Higher temperatures can be used in later experiments to approach the HEL more closely and, eventually, investigate the probable effect of defect annealing.

Finally, we point out that EDXRD and Raman spectroscopy are complementary, and in our view both of them should systematically be used in the study of damage in boron carbide. The probable occurrence of amorphous zones could be detected, however further theoretical and experimental investigations are required to understand their formation mechanism(s).

Acknowledgement

Supports from the DGA (France) and from the program NEEDS-Matériaux (France) are gratefully acknowledged. The authors thank Benoit Baptiste, Ludovic Delbes and Hicham Moutaabbid for useful discussions. Fruitful discussions with Guido Roma and Gaëlle Gutierrez are also acknowledged. The authors also thank Dr. Nicolas Guignot of PSICHE beamline in SOLEIL synchrotron. The Raman spectroscopy platform in IMPMC is also acknowledged. The PhD fellowship for A. Chakraborti has been provided by the Ecole Doctorale of Institut Polytechnique de Paris. This work was granted access to high performance computing resources by the Partnership for Advanced Computing in Europe (PRACE Project No. 2019204962), by the French HPC centers GENCI-IDRIS, GENCI-CINES and GENCI-TGCC (Project 2210) and by Ecole Polytechnique through the 3L-hpc project. Financial support from the DIM SIRTEQ (région Ile de France) is gratefully acknowledged.

References

[1] M. Herrmann, I. Sigalas, M. Thiele, M. Müller, H. J. Kleebe, A. Michaelis, Boron suboxide ultrahard materials, International Journal of Refractory Metals and Hard Materials 39 (2013) 53–60.

[2] F. Thévenot, Boron carbide—a comprehensive review, Journal of the European Ceramic Society 6 (1990) 205–225.

[3] G. Fanchini, J. W. McCauley, M. Chhowalla, Behavior of disordered boron carbide under stress, Phys. Rev. Lett. 97 (2006) 035502.

[4] G. R. Johnson, T. J. Holmquist, Response of boron carbide subjected to large strains, high strain rates, and high pressures, Journal of Applied Physics 85 (1999) 8060–8073.

[5] V. Domnich, S. Reynaud, R. A. Haber, M. Chhowalla, Boron carbide: Structure, properties, and stability under stress, Journal of the American Ceramic Society 94 (2011) 3605–3628.

[6] for a discussion, see section V of ref. Domnich *et al.*, 2011.

[7] A. Hushur, M. H. Manghnani, H. Werheit, P. Dera, Q. Williams, High-pressure phase transition makes $B_{4.3}C$ boron carbide a wide-gap semiconductor, Journal of Physics: Condensed Matter 28 (2016) 045403.

[8] T. J. Vogler, W. D. Reinhart, L. C. Chhabildas, Dynamic behavior of boron carbide, Journal of Applied Physics 95 (2004) 4173–4183.

[9] W. D. Reinhart, L. C. Chhabildas, T. J. Vogler, Investigating phase transitions and strength in single-crystal sapphire using shock–reshock loading techniques, International Journal of Impact Engineering 33 (2006) 655–669.

[10] N. C. Zhang, F. S. Liu, W. P. Wang, Y. Y. Sun, Q. J. Liu, X. J. Peng, J. X. Chen, Shock-induced optical emission and high-pressure phase transformation of sapphire, Physica B: Condensed Matter 429 (2013) 90–94.

[11] X. Cao, Y. Wang, X. Li, L. Xu, L. Liu, Y. Yu, R. Qin, W. Zhu, S. Tang, L. He, C. Meng, B. Zhang, X. Peng, Refractive index and phase transformation of sapphire under shock pressures up to 210 GPa, Journal of Applied Physics 121 (2017) 115903.

[12] T. Goto, Y. Syono, J. Nakai, Y. Nakagawa, Pressure-induced phase transition in GaAs under shock compression, Solid State Communications 18 (1976) 1607–1609.

[13] S. Ono, T. Kikegawa, Phase transformation of GaAs at high pressures and temperatures, Journal of Physics and Chemistry of Solids 113 (2018) 1–4.

[14] S. K. Sikka, Behaviour of materials under shock loading conditions, Bulletin of Materials Science 15 (1) (1992) 35–46.

[15] P. Dera, M. H. Manghnani, A. Hushur, Y. Hu, S. Tkachev, New insights into the enigma of boron carbide inverse molecular behavior, Journal of Solid State Chemistry 215 (2014) 85–93.

[16] H. Werheit, M. H. Manghnani, U. Kuhlmann, A. Hushur, S. Shalamberidze, Mode Grüneisen parameters of boron carbide, Solid State Sciences 72 (2017) 80–93.

[17] H. Werheit, Comment on: Structural stability of boron carbide under pressure proven by spectroscopic studies up to 73 GPa (z. anorg. allg. chem. 643, 1357 (2017)), Zeitschrift für anorganische und allgemeine Chemie 644 (2018) 353–356.

[18] H. Werheit, M. H. Manghnani, A. Hushur, Phonon peculiarities at the high-pressure phase transition of $B_{4.3}C$ boron carbide, Solid State Sciences 97 (2019) 105978.

[19] H. Werheit, Assignment of the electronic transitions in $B_{4.3}C$ boron carbide implies a specifically distorted crystal structure, Solid State Sciences 86 (2018) 38–44.

[20] A. Ektarawong, S. I. Simak, L. Hultman, J. Birch, B. Alling, First-principles study of configurational disorder in B_4C using a superatom-special quasirandom structure method, Physical Review B 90 (2014) 024204.

[21] K. M. Reddy, P. Liu, A. Hirata, T. Fujita, M. W. Chen, Atomic structure of amorphous shear bands in boron carbide, Nature Communications 4 (2013) 2483.

[22] G. Subhash, D. Ghosh, J. Blaber, J. Q. Zheng, V. Halls, K. Masters, Characterization of the 3-D amorphized zone beneath a Vickers indentation in boron carbide using Raman spectroscopy, Acta Materialia 61 (2013) 3888–3896.

[23] M. Chen, J. W. McCauley, K. J. Hemker, Shock-induced localized amorphization in boron carbide, Science 299 (2003) 1563.

[24] X. Q. Yan, Z. Tang, L. Zhang, J. J. Guo, C. Q. Jin, Y. Zhang, T. Goto, J. W. McCauley, M. W. Chen, Depressurization amorphiza-

tion of single-crystal boron carbide, Physical Review Letters 102 (2009) 075505.

[25] D. Ghosh, G. Subhash, J. Q. Zheng, V. Halls, Influence of stress state and strain rate on structural amorphization in boron carbide, Journal of Applied Physics 111 (2012) 063523.

[26] A. Awasthi, G. Subhash, Deformation behavior and amorphization in icosahedral boron-rich ceramics, Progress in Materials Science 112 (2020) 100664.

[27] R. Raucoules, N. Vast, E. Betranhandy, J. Sjakste, Mechanical properties of icosahedral boron carbide explained from first principles, Physical Review B 84 (2011) 014112.

[28] A. Jay, *In Silico* design of a new phase of boron carbide, Ph.D. thesis, École Polytechnique, Palaiseau (2014).

[29] J. Rabier, L. Pizzagalli, J. Demenet, Dislocations in Solids, Elsevier, 2010.

[30] D. Hull, D. Bacon, Introduction to Dislocations, 5th Edition, Elsevier, Amsterdam, New York, 2011.

[31] M. Iyer, V. Gavini, T. M. Pollock, Energetics and nucleation of point defects in aluminum under extreme tensile hydrostatic stresses, Physical Review B 89 (2014) 014108.

[32] T. J. Holmquist, G. R. Johnson, Characterization and evaluation of boron carbide for plate-impact conditions, Journal of Applied Physics 100 (2006) 093525.

[33] J. Philippe, Y. Le Godec, M. Mezouar, M. Berg, G. Bromiley, F. Bergame, J. P. Perrillat, M. Alvarez-Murga, M. Morand, R. Atwood, A. King, S. Régnier, Rotating tomography Paris-Edinburgh cell: a novel portable press for micro-tomographic 4-D imaging at extreme pressure/temperature/stress conditions, High Pressure Research 36 (2016) 512–532.

[34] H. F. Fischmeister, E. Arzt, L. R. Olsson, Particle deformation and sliding during compaction of spherical powders: A study by quantitative metallography, Powder Metallurgy 21 (1978) 179–187.

[35] W. Zhang, A review of tribological properties for boron carbide ceramics, Progress in Materials Science 116 (2021) 100718.

[36] W. Zhang, S. Yamashita, H. Kita, Effects of load on tribological properties of B_4C and B_4C-SiC ceramics sliding against SiC balls, Journal of Asian Ceramic Societies 8 (2020) 586–596.

[37] K. Cherednichenko, Boron chalcogenides under extreme conditions, Ph.D. thesis, Université Pierre et Marie Curie - Paris VI (2015).

[38] A. Chakraborti, N. Vast, Y. Le Godec, Synthesis of boron carbide from its elements at high pressures and high temperatures, Solid State Sciences 104 (2020) 106265.

[39] A. Chakraborti, N. Guignot, N. Vast, Y. Le Godec, Synthesis of boron carbide from its elements up to 13 GPa, Journal of Physics and Chemistry of Solids 159 (2021) 110253.

[40] A. Jay, O. Hardouin Duparc, J. Sjakste, N. Vast, Theoretical phase diagram of boron carbide from ambient to high pressure and temperature, Journal of Applied Physics 125 (2019) 185902.

[41] M. N. Pavlovsky, Shock compressibility of six very hard substances, Sov. Phys. Solid State 12 (1971) 1736.

[42] D. P. Dandekar, Shock response of boron carbide, Tech. rep., Army Research Laboratory, Aberdeen Proving Ground, Aberdeen, Maryland, USA (2001).

[43] M. DeVries, G. Subhash, A. Awasthi, Shocked ceramics melt: An atomistic analysis of thermodynamic behavior of boron carbide, Phys. Rev. B 101 (2020) 144107.

[44] We note that a possible annealing of defects due to the elevated temperature in the shock wave experiments has not been considered in the above estimation of the pressure.

[45] H. Werheit, A. Leithe-Jasper, T. Tanaka, H. W. Rotter, K. A. Schwetz, Some properties of single-crystal boron carbide, Journal of Solid State Chemistry 177 (2004) 575–579.

[46] H. Werheit, R. Schmechel, U. Kuhlmann, T. U. Kampen, W. Mönch, A. Rau, On the reliability of the Raman spectra of boron-rich solids, Journal of Alloys and Compounds 291 (1999) 28–32.

[47] H. Werheit, Systematic error in conventionally measured Raman spectra of boron carbide—a general issue in solid state Raman spectroscopy, Review of Scientific Instruments 90 (2019) 043114.

[48] G. Roma, K. Gillet, A. Jay, N. Vast, G. Gutierrez, Understanding first order Raman spectra of boron carbides across the homogeneity range, Phy. Rev. Mat 5 (2021) 4063601.

[49] H. Werheit, Comment on: Understanding first order Raman spectra of boron carbides across the homogeneity range by Roma *et al.*, Physical Review Materials to be published (2021).

[50] G. Roma, A. Jay, N. Vast, O. Hardouin Duparc, G. Gutierrez, Reply to "Comment on 'Understanding first order Raman spectra of boron carbides across the homogeneity range"', Physical Review Materials to be published (2021).

[51] K. Y. Xie, V. Domnich, L. Farbaniec, B. Chen, K. Kuwelkar, L. Ma, J. W. McCauley, R. A. Haber, K. T. Ramesh, M. Chen, K. J. Hemker, Microstructural characterization of boron-rich boron carbide, Acta Materialia 136 (2017) 202–214.

[52] P. Hohenberg, W. Kohn, Inhomogeneous electron gas, Phys. Rev. 136 (1964) B864–B871.

[53] W. Kohn, L. J. Sham, Self-consistent equations including exchange and correlation effects, Phys. Rev. 140 (1965) A1133–A1138.

[54] S. Baroni, S. de Gironcoli, A. Dal Corso, P. Giannozzi, Phonons and related crystal properties from density-functional perturbation theory, Rev. Mod. Phys. 73 (2001) 515–562.

[55] J. P. Perdew, Y. Wang, Accurate and simple analytic representation of the electron-gas correlation energy, Physical Review B 45 (1992) 13244–13249.

[56] J. P. Perdew, A. Zunger, Self-interaction correction to density-functional approximations for many-electron systems, Physical Review B 23 (1981) 5048–5079.

[57] R. Lazzari, N. Vast, J. M. Besson, S. Baroni, A. Dal Corso, Atomic structure and vibrational properties of icosahedral B_4C boron carbide, Phys. Rev. Lett. 83 (1999) 3230–3233.

[58] A. Jay, N. Vast, J. Sjakste, O. Hardouin Duparc, Carbon-rich icosahedral boron carbide designed from first principles, Applied Physics Letters 105 (2014) 031914.

[59] H. J. Monkhorst, J. D. Pack, Special points for Brillouin-zone integrations, Physical Review B 13 (1976) 5188–5192.

[60] M. Methfessel, A. T. Paxton, High-precision sampling for Brillouin-zone integration in metals, Physical Review B 40 (1989) 3616–3621.

[61] L. R. Pratt, A statistical method for identifying transition states in high dimensional problems, The Journal of Chemical Physics 85 (1986) 5045–5048.

[62] R. Elber, M. Karplus, A method for determining reaction paths in large molecules: Application to myoglobin, Chemical Physics Letters 139 (1987) 375–380.

[63] E. Betranhandy, N. Vast, J. Sjakste, Ab initio study of defective chains in icosahedral boron carbide B_4C, Solid State Sciences 14 (2012) 1683–1687.

[64] N. Vast, J. Sjakste, E. Betranhandy, Boron carbides from first principles 176 (2009) 012002.

[65] K. Gillet, G. Roma, J.-P. Crocombette, D. Gosset, The influence of irradiation induced vacancies on the mobility of helium in boron carbide, Journal of Nuclear Materials 512 (2018) 288–296.

[66] F. Mauri, N. Vast, C. J. Pickard, Atomic structure of icosahedral B_4C boron carbide from a first principles analysis of NMR spectra, Physical Review Letters 87 (2001) 085506.

[67] M. M. Balakrishnarajan, P. D. Pancharatna, R. Hoffmann, Structure and bonding in boron carbide: The invincibility of imperfections, New Journal of Chemistry 31 (2007) 473–485.

[68] K. C. Pandey, Diffusion without vacancies or interstitials: A new concerted exchange mechanism, Physical Review Letters 57 (1986) 2287–2290.

[69] B. Morosin, T. L. Aselage, R. S. Feigelson, Crystal structure refinements of rhombohedral symmetry materials containing boron-rich icosahedra, in: MRS Proceedings, Vol. 97, Cambridge University Press, 1987, p. 145.

[70] S. Inoue, S. Fukuda, T. Hino, T. Yamashina, Change of surface composition of B_4C single crystal due to heat treatment, Journal of Vacuum Science Technology A 5 (1987) 1279–1282.

[71] C. Pallier, Evolution structural des céramiques (Si)-B-C sous sollications thermomécaniques., Ph.D. thesis, Université Bordeaux (2012).

[72] C. Pallier, J.-M. Leyssale, L. Truflandier, A. T. Bui, W. P, C. Gervais, H. Fischer, F. Sirotti, F. Teyssandier, G. Chollon, Structure of an amorphous boron carbide film: An experimental and computational approach, Chemistry of Materials 25 (2013) 2618–2629.

[73] D. Gosset, S. Miro, S. Doriot, G. Victor, V. Motte, Evidence of amorphisation of B_4C boron carbide under slow, heavy ion irradiation, Nuclear Instruments and Methods in Physics Research Section B: Beam Interactions with Materials and Atoms 365 (2015) 300–304.

[74] G. Victor, Y. Pipon, N. Bérerd, N. Toulhoat, N. Moncoffre, N. Djourelov, S. Miro, J. Baillet, N. Pradeilles, O. Rapaud, A. Maître, D. Gosset, Structural modifications induced by ion irradiation and temperature in boron carbide B_4C, Nuclear Instruments and Methods in Physics Research Section B: Beam Interactions with Materials and Atoms 365 (2015) 30–34.

[75] D. Gosset, S. Miro, S. Doriot, N. Moncoffre, Amorphisation of boron carbide under slow heavy ion irradiation, Journal of Nuclear Materials 476 (2016) 198–204.

[76] A. P. Awasthi, G. Subhash, High-pressure deformation and amorphization in boron carbide, Journal of Applied Physics 125 (2019) 215901.

[77] M. Marton, M. Vojs, E. Zdravecká, M. Himmerlich, T. Haensel, S. Krischok, M. Kotlár, P. Michniak, M. Veselý, R. Redhammer, Raman spectroscopy of amorphous carbon prepared by pulsed arc discharge in various gas mixtures, Journal of Spectroscopy 2013 (2013) 467079.

[78] C. Kunka, A. Awasthi, G. Subhash, Evaluating boron-carbide constituents with simulated raman spectra, Scripta Materialia 138 (2017) 32–34.

[79] U. Kuhlmann, H. Werheit, On the microstructure of boron carbide, Solid State Communications 83 (1992) 849–852.

[80] V. I. Ivashchenko, V. I. Shevchenko, P. E. A. Turchi, First-principles study of the atomic and electronic structures of crystalline and amorphous b_4C, Physical Review B 80 (2009) 235208.

Declaration of interests

☒ The authors declare that they have no known competing financial interests or personal relationships that could have appeared to influence the work reported in this paper.

☐ The authors declare the following financial interests/personal relationships which may be considered as potential competing interests: